EUROFUSION WP15ER-PR(16) 15799

C Slaby et al.

Numerical investigation of non-perturbative kinetic effects of energetic particles on toroidicity-induced Alfven eigenmodes in tokamaks and stellarators

Preprint of Paper to be submitted for publication in
Physics of Plasmas

This work has been carried out within the framework of the EUROfusion Consortium and has received funding from the Euratom research and training programme 2014-2018 under grant agreement No 633053. The views and opinions expressed herein do not necessarily reflect those of the European Commission.

Numerical investigation of non-perturbative kinetic effects of energetic particles on toroidicity-induced Alfvén eigenmodes in tokamaks and stellarators

Christoph Slaby, Axel Könies, and Ralf Kleiber
Max-Planck-Institut für Plasmaphysik,
D-17491 Greifswald, Germany

(Dated: March 7, 2016)

Abstract

The resonant interaction of shear Alfvén waves with energetic particles is investigated numerically in tokamak and stellarator geometry using a non-perturbative MHD-kinetic hybrid approach. The focus lies on toroidicity-induced Alfvén eigenmodes (TAEs), which are most easily destabilized by a fast-particle population in fusion plasmas.

While the background plasma is treated within the framework of ideal-MHD theory, the drive of the fast particles, as well as Landau damping of the background plasma, is modelled using the drift-kinetic Vlasov equation without collisions. A fast numerical tool, STAE-K, has been developed to solve the resulting eigenvalue problem using a Riccati shooting method. The code, which is suitable for parameter scans, is applied to tokamaks and the stellarator Wendelstein 7-X.

Energetic particle modes (EPMs) are found when the pressure of the energetic particles becomes comparable to the pressure of the background plasma. To better understand the physics of EPMs, the connections between TAEs and the shear Alfvén wave continuum are examined. It is shown that, when energetic particles are present, the continuum deforms substantially and the TAE frequency can leave the continuum gap. The interaction of the TAE with the continuum leads to singularities in the eigenfunctions. To further advance the physical model and also to eliminate the MHD continuum together with the singularities in the eigenfunctions, a fourth-order term connected to radiative damping has been included. The radiative damping term is connected to non-ideal effects of the bulk plasma and introduces higher-order derivatives to the model. Thus, it has the potential to substantially change the nature of the solution.

For the first time, the fast-particle drive, Landau damping, continuum damping, and radiative damping have been modelled together in tokamak- as well as in stellarator geometry.

I. INTRODUCTION

In a burning fusion plasma, alpha particles are produced with a velocity that exceeds the typical Alfvén speed. In the process of slowing down, these fast particles may transfer energy to Alfvén waves, which thus become unstable [1, 2]. Also heating methods such as ion cyclotron resonance heating (ICRH) and neutral beam injection (NBI) can supply energetic particles with similar consequences. The resonant interaction of the fast particles with Alfvén waves, in particular with toroidicity-induced Alfvén eigenmodes (TAEs), may lead to a degraded confinement of the energetic particles and thereby to particle loss and high heat loads on the first-wall components [3, 4]. In particular, an energetic particle mode (EPM), determined by the properties of the energetic particle distribution function, may form [5].

In this paper, the resonant particle-wave interaction is studied analytically and numerically using a non-perturbative MHD-kinetic hybrid model in which the background plasma is modelled using ideal-MHD theory, whereas the fast particles are treated kinetically.

To assess the stability or instability of a given mode, various damping mechanisms such as Landau damping, radiative damping and continuum damping are just as important as the kinetic drive of the energetic particle species [6]. Therefore, a numerical tool, namely a shooting code for toroidicity-induced Alfvén eigenmodes with kinetic extensions (STAE-K), has been developed, which is able to take into account all these different stabilizing and destabilizing contributions (but cannot completely describe collisional damping). The equations are solved in tokamak- (circular flux surfaces) or stellarator geometry in the large-aspect-ratio and low-beta approximation.

The structure of the paper is as follows. First, the MHD-kinetic hybrid model will be introduced by discussing the MHD and the kinetic part separately. The numerical methods employed and the implementation of the model will be described in Sec. III. After the shooting code is benchmarked in Sec. IV, further results will be presented in Sec. V. Finally, conclusions are drawn in Sec. VI.

The two appendices elaborate on details of the theory outlined in Sec. II and summarize the various background-plasma and fast-particle parameters used in the numerical calculations, respectively.

II. THEORY

In this section a simple MHD-kinetic hybrid model will be developed, which is well suited for fast and efficient numerical calculations. To this end, some simplifying assumptions are made: For both the tokamak or stellarator, large-aspect-ratio devices are considered. This simplifies the metric tensor, because only first-order corrections due to toroidicity and helical shaping have to be taken into account. In addition, a low-beta plasma is assumed, and only shear Alfvén waves are included in this analysis by taking $\mathbf{A}^{(1)} = A_{\parallel}^{(1)}\mathbf{b}$, where $\mathbf{A}$ is the vector potential and $\mathbf{b}$ is the unit vector along the magnetic field $\mathbf{B}$. In the following, the superscripts $^{(0)}$ and $^{(1)}$ will be used to label equilibrium and perturbed quantities, respectively. The symbols $_{\parallel}$ and $_{\perp}$ indicate vector components

parallel or perpendicular to the direction of the equilibrium magnetic field. The perturbations, which are assumed to be much smaller than the equilibrium quantities, are supposed to vary in time as $\exp(-\mathrm{i}\omega t)$ with the mode frequency $\omega \in \mathbb{C}$.
In order to improve the performance of the numerical implementation, as many calculations as possible are performed on an analytical level.
The eigenmode equation is derived from the quasi-neutrality condition $\nabla \cdot \mathbf{j}^{(1)} = 0$, which can be split into an MHD part and the kinetic contribution of the fast particles

$$\nabla \cdot \mathbf{j}^{(1)}_{\mathrm{MHD}} + \nabla \cdot \mathbf{j}^{(1)}_{\mathrm{fast}} = 0. \tag{1}$$

Here, the perturbed energetic-particle current density can be calculated using

$$\mathbf{j}^{(1)}_{\mathrm{fast}} = Z_{\mathrm{fast}}\mathrm{e} \int \mathrm{d}^3v \; f^{(1)} \mathbf{v}_{\mathrm{D}} + \nabla \times \mathbf{m}^{(1)}_{\mathrm{fast}} \tag{2}$$

with $f^{(1)}$ being the perturbed distribution function of the kinetically treated fast-particle species and $\mathbf{v}_{\mathrm{D}}$ being their drift velocity ($Z_{\mathrm{fast}}\mathrm{e}$ is the charge of the fast particles). The second term on the right-hand side of Eq. (2) is the magnetization current of the fast particles [7], which is unimportant, because it is divergence-free. In the following, the two terms in Eq. (1) will be discussed separately.

A. MHD part

As the MHD-terms of the model have already been derived by others [8–10], those calculations need not be repeated in the present paper. Thus, just a brief overview is given here.
The linearized MHD momentum equation is used to solve for $\mathbf{j}^{(1)}_{\perp}$. Using Maxwell's equations gives

$$\nabla \cdot \mathbf{j}^{(1)}_{\mathrm{MHD}} = \left(\mathbf{B}^{(0)} \cdot \nabla\right) \left(\frac{\mathbf{B}^{(0)} \cdot \mathbf{j}^{(1)}}{B^2}\right) + \left(\mathbf{B}^{(1)}_{\perp} \cdot \nabla\right) \left(\frac{\mathbf{B}^{(0)} \cdot \mathbf{j}^{(0)}}{B^2}\right) + \frac{\mathrm{i}\omega}{\mu_0} \nabla \cdot \left(\frac{\nabla_{\perp} \Phi^{(1)}}{v_{\mathrm{A}}^2}\right), \tag{3}$$

if the perturbed plasma flow is approximated by the $\mathbf{E} \times \mathbf{B}$-drift. Here, $v_{\mathrm{A}} = B/\sqrt{\mu_0 n_{\mathrm{i}} m_{\mathrm{i}}}$ is the Alfvén velocity of the background-plasma ions with mass m_{i} and density n_{i}. μ_0 is the vacuum permeability and the electric potential is denoted by Φ. Following Ref. [9] the term with the equilibrium current density is dropped for simplicity in the case of stellarators like Wendelstein 7-X (W7-X).
In the large-aspect-ratio and small-plasma-beta limit several possible simplifications of Eq. (3) have been discussed extensively in Ref. [8]. They involve expressing $\mathbf{B}^{(0)} \cdot \mathbf{j}^{(1)}$ and $\mathbf{B}^{(1)}_{\perp}$ in terms of the perturbed vector potential. The ideal-MHD condition $E_{\parallel} = 0$ leads to $\mathrm{i}\omega A^{(1)}_{\parallel} = (\mathbf{b} \cdot \nabla)\Phi^{(1)}$ and provides the necessary connection to $\Phi^{(1)}$. After using

these simplifications a Fourier transform finally leads to

$$\begin{aligned}\mathcal{FT}\left(\frac{\mathrm{i}\omega\mu_0\sqrt{g}}{rR_0}\nabla\cdot\mathbf{j}^{(1)}_{\mathrm{MHD}}\right) = \\ = \left[\frac{1}{r}\frac{\mathrm{d}}{\mathrm{d}r}r\left(k^2_{m,n}-\frac{\omega^2}{v^2_{\mathrm{A}}}\right)\frac{\mathrm{d}}{\mathrm{d}r}-\frac{1}{r}\left(\frac{\mathrm{d}}{\mathrm{d}r}k^2_{m,n}\right)-\frac{m^2}{r^2}\left(k^2_{m,n}-\frac{\omega^2}{v^2_{\mathrm{A}}}\right)\right]\Phi^{(1)}_m + \\ + \left[-\frac{2}{r}\frac{\mathrm{d}}{\mathrm{d}r}r\frac{\omega^2}{v^2_{\mathrm{A}}}\left(\Delta'+\frac{r}{R_0}\right)\frac{\mathrm{d}}{\mathrm{d}r}-\frac{2}{r^2}\frac{\omega^2}{v^2_{\mathrm{A}}}\Delta' m\left(m+1\right)\right]\Phi^{(1)}_{m+1} + \\ + \left[-\frac{2}{r}\frac{\mathrm{d}}{\mathrm{d}r}r\frac{\omega^2}{v^2_{\mathrm{A}}}\left(\Delta'+\frac{r}{R_0}\right)\frac{\mathrm{d}}{\mathrm{d}r}-\frac{2}{r^2}\frac{\omega^2}{v^2_{\mathrm{A}}}\Delta' m\left(m-1\right)\right]\Phi^{(1)}_{m-1},\end{aligned} \tag{4}$$

where $\sqrt{g}$ is the determinant of the metric tensor used in Ref. [8] and $k_{m,n} = (n - m/q)/R_0$ denotes the parallel wave vector with poloidal and toroidal mode numbers m and n, respectively. R_0 is the major radius of the toroidal device and $q = 1/\iota$ is the safety factor (ι being the rotational transform). The Shafranov shift is denoted by Δ, and primes label a derivative with respect to the radial variable r.
An equation very similar to Eq. (4) has been derived in Ref. [9] for stellarators

$$\begin{aligned}\mathcal{FT}\left(\frac{\mathrm{i}\omega\mu_0 r^2}{\alpha^2\delta_0}\nabla\cdot\mathbf{j}^{(1)}_{\mathrm{MHD}}\right) = Q_{m,n}\Phi^{(1)}_{m,n} + \frac{1}{r^2}\frac{\mathrm{d}}{\mathrm{d}r}r^3\Bigg\{\left(k^2_{m,n}-\frac{\omega^2}{v^2_{\mathrm{A}}}\right)\left(\frac{1}{r}\frac{\mathrm{d}}{\mathrm{d}r}-\frac{1}{r^2}\right)\Phi^{(1)}_{m,n} + \\ + \sum_{\mu,\nu}\left[k_{m,n}k_{m+\mu,n+\nu N_{\mathrm{P}}}\frac{\epsilon^{(\mu,\nu)}_{\mathrm{g}}}{2}-\frac{\omega^2}{v^2_{\mathrm{A}}}\epsilon^{(\mu,\nu)}\right]\left(\frac{1}{r}\frac{\mathrm{d}}{\mathrm{d}r}-\frac{1}{r^2}\right)\Phi^{(1)}_{m+\mu,n+\nu N_{\mathrm{P}}} + \\ + \sum_{\mu,\nu}\left[k_{m,n}k_{m-\mu,n-\nu N_{\mathrm{P}}}\frac{\epsilon^{(\mu,\nu)}_{\mathrm{g}}}{2}-\frac{\omega^2}{v^2_{\mathrm{A}}}\epsilon^{(\mu,\nu)}\right]\left(\frac{1}{r}\frac{\mathrm{d}}{\mathrm{d}r}-\frac{1}{r^2}\right)\Phi^{(1)}_{m-\mu,n-\nu N_{\mathrm{P}}}\Bigg\}.\end{aligned} \tag{5}$$

Here, $\epsilon^{(\mu,\nu)} = \epsilon^{(\mu,\nu)}_{\mathrm{g}}/2 - 2\epsilon^{(\mu,\nu)}_{\mathrm{B}}$ determines the strength of the mode coupling due to geometry. It is given in the following representations for the rr-component of the metric tensor

$$g^{rr} = \delta_0\left[1+\sum_{\mu,\nu}\epsilon^{(\mu,\nu)}_{\mathrm{g}}\cos\left(\mu\Theta-\nu N_{\mathrm{P}}\varphi\right)\right] \tag{6}$$

(δ_0 is connected to the elongation of the plasma) and for the magnetic field strength [9]

$$B = B_0\left[1+\sum_{\mu,\nu}\epsilon^{(\mu,\nu)}_{\mathrm{B}}\cos\left(\mu\Theta-\nu N_{\mathrm{P}}\varphi\right)\right] = B_0\alpha. \tag{7}$$

μ and ν characterise the mode coupling in poloidal and toroidal direction, respectively. The corresponding angles are Θ and φ, and N_{P} denotes the number of field periods. Furthermore,

$$Q_{m,n} = \frac{1}{r^2}\left(k^2_{m,n}-\frac{\omega^2}{v^2_{\mathrm{A}}}\right)\left(1-m^2\right) - \frac{1}{r}\frac{\mathrm{d}}{\mathrm{d}r}\left(\frac{\omega^2}{v^2_{\mathrm{A}}}\right). \tag{8}$$

Taking into account only the toroidal coupling $\mu = 1, \nu = 0$ reduces Eq. (5) to its tokamak equivalent, Eq. (4) [11].
In any case, a coupled system of ordinary second-order differential equations in r has to be solved. The system becomes larger the more poloidal (and toroidal) modes of $\Phi^{(1)}$ are taken into account.

B. Fast-particle part

The contribution of the energetic particles to Eq. (1) is given by

$$\nabla \cdot \mathbf{j}^{(1)}_{\text{fast}} = Z_{\text{fast}} \mathrm{e} \int \mathrm{d}^3 v \, \nabla \cdot \left(f^{(1)} \mathbf{v}_{\mathrm{D}} \right) \cong Z_{\text{fast}} \mathrm{e} \int \mathrm{d}^3 v \, \nabla \cdot \left(h^{(1)} \mathbf{v}_{\mathrm{D}} \right). \tag{9}$$

Note that the perturbed fast-particle distribution function can be approximated by its non-adiabatic part $h^{(1)}$ because the particle-wave resonance condition is only contained in $h^{(1)}$ [12]. The adiabatic part of $f^{(1)}$, on the other hand, would only contribute to the fluid part. $h^{(1)}$ is given by

$$\begin{aligned} h^{(1)}_{m,n} = \frac{Z_{\text{fast}} \mathrm{e} \, v_{\mathrm{D},0}}{2} \frac{1}{\omega - v_{\parallel} k_{m,n}} \frac{\partial F}{\partial \varepsilon} \left(1 - m \frac{\omega_\star}{\omega} \right) \times \\ \times \left[\left\{ \frac{\mathrm{d}}{\mathrm{d}r} - \frac{m-1}{r} \right\} \Phi^{(1)}_{m-1} - \left\{ \frac{\mathrm{d}}{\mathrm{d}r} + \frac{m+1}{r} \right\} \Phi^{(1)}_{m+1} \right] \end{aligned} \tag{10}$$

for tokamaks [8]. Here, $v_{\mathrm{D},0}$ is the magnitude of the toroidal drift at $r = 0$, and F is the Maxwellian equilibrium distribution function of the fast particles, whose kinetic energy is denoted by ε. $\omega_\star$ is their diamagnetic drift frequency defined as

$$\omega_\star = \frac{\partial F / \partial r}{\partial F / \partial \varepsilon} \frac{1}{M \Omega_0 r}, \tag{11}$$

with mass M and on-axis gyration frequency Ω_0. Note that for stellarators Eq. (10) is generalized to

$$\begin{aligned} h^{(1)}_{m,n} = \frac{R_0 Z_{\text{fast}} \mathrm{e} \, v_{\mathrm{D},0}}{2r} \frac{1}{\omega - v_{\parallel} k_{m,n}} \frac{\partial F}{\partial \varepsilon} \Bigg[\left(1 - m \frac{\omega_\star}{\omega} \right) \times \\ \times \Bigg\{ \sum_{\mu,\nu} \frac{\mathrm{d}\epsilon^{(\mu,\nu)}_{\mathrm{B}}}{\mathrm{d}r} \left[(m-\mu) \, \Phi^{(1)}_{m-\mu,n-\nu N_{\mathrm{P}}} + (m+\mu) \, \Phi^{(1)}_{m+\mu,n+\nu N_{\mathrm{P}}} \right] + \\ - \sum_{\mu \neq 0,\nu} \epsilon^{(\mu,\nu)}_{\mathrm{B}} \frac{\mathrm{d}}{\mathrm{d}r} \left[\Phi^{(1)}_{m-\mu,n-\nu N_{\mathrm{P}}} - \Phi^{(1)}_{m+\mu,n+\nu N_{\mathrm{P}}} \right] \Bigg\} \Bigg]. \end{aligned} \tag{12}$$

After some straightforward algebra, where it must be pointed out that the integration over velocity space in Eq. (9) has been performed analytically for the Maxwellian F, one arrives also for the fast particles at a coupled system of second-order differential equations in r. The resulting equation for $\nabla \cdot \mathbf{j}^{(1)}_{\text{fast}}$ is given in Appendix A for the stellarator case.

C. Radiative damping

Up to now the model only contains second-order differential operators. Radiative damping by the background-plasma is described by a fourth-order operator [13, 14]. Here, a term derived in Ref. [13] that takes into account finite-Larmor-radius effects as well as a parallel electric field that arises due to the kinetic modelling of the electron dynamics will be included. This term enables the coupling of TAEs to kinetic Alfvén waves and opens up a new energy loss channel, i.e. damps the TAEs. Following Ref. [13], this term is added to Eq. (1) and reads as

$$D = \nabla \cdot \left[\nabla_\perp \left\{ d_{\mathrm{rad}} \frac{1}{m_\mathrm{i} n_\mathrm{i}} \nabla \cdot \left(m_\mathrm{i} n_\mathrm{i} \nabla_\perp \Phi^{(1)} \right) \right\} \right] \tag{13}$$

with

$$d_{\mathrm{rad}} = k_{m,n}^2 \left[\frac{3}{4} \rho_\mathrm{i}^2 + \rho_\mathrm{s}^2 \frac{1 + \mathrm{i}\hat{\nu} Z\left(x\right)}{1 + x Z\left(x\right)} \right] \tag{14}$$

and

$$x = \frac{\omega + \mathrm{i}\nu}{k_{m,n} v_{\mathrm{th,e}}}, \tag{15}$$

where $\rho_\mathrm{i} = \sqrt{k_\mathrm{B} T_\mathrm{i} m_\mathrm{i}}/(Z_\mathrm{i} \mathrm{e} B)$ is the ion gyroradius, $\rho_\mathrm{s} = \sqrt{k_\mathrm{B} T_\mathrm{e} m_\mathrm{i}}/(Z_\mathrm{i} \mathrm{e} B)$ is the sound gyroradius, and $\hat{\nu} = \nu/(k_{m,n} v_{\mathrm{th,e}})$ is a normalized collision frequency with ν being the electron-ion collision frequency. $v_{\mathrm{th,e}} = \sqrt{2 k_\mathrm{B} T_\mathrm{e}/m_\mathrm{e}}$ is the electron thermal velocity and Z is the well-known plasma dispersion function [15].
Subsequently, the radiative damping term is treated under the assumption that the derivatives do not act on the equilibrium quantities, i.e.

$$D \cong d_{\mathrm{rad}} \left(\nabla \cdot \nabla_\perp \right)^2 \Phi^{(1)}, \tag{16}$$

implying that the equilibrium does not change much over the radial extent of the mode. It then only remains to perform a Fourier transform of the simplified term, taking into account the poloidal dependence (given by the metric tensor components) of $(\nabla \cdot \nabla_\perp)^2$ in either tokamak or stellarator geometry. This yields a coupled system of differential equations in r, but now every single equation is of fourth order.

III. NUMERICAL IMPLEMENTATION

A. General scheme

Depending on whether radiative damping is taken into account, a system of second-order or fourth-order ordinary differential equations in the radial variable r has to be solved. Considering, for simplicity, a tokamak with the fourth-order radiative damping term being present, results in the following system of equations (with the superscript $^{(1)}$ omitted from this point on)

$$M_4 \boldsymbol{\Phi}^{(\mathrm{iv})} + M_3 \boldsymbol{\Phi}''' + M_2 \boldsymbol{\Phi}'' + M_1 \boldsymbol{\Phi}' + M_0 \boldsymbol{\Phi} = \mathbf{0}, \tag{17}$$

which is obtained by combining Eq. (4) with the Fourier transformed versions of Eq. (9) (see Appendix A) and Eq. (16). The M_i, $(i = 0, \ldots, 4)$ are complex $\Delta m \times \Delta m$-matrices, and the vector $\mathbf{\Phi} = (\phi_{m,n}, \ldots, \phi_{m+\Delta m,n})^{\mathrm{T}}$ contains the Δm poloidal modes of the perturbed electric potential that are taken into account. For a stellarator there would be an additional variation in the toroidal mode number n, leading to a larger system.
One aim of the STAE-K code is to survey the importance of EPMs by conducting parameter scans (e.g. varying the fast-particle temperature or the fast-particle density). Therefore, a shooting code making use of the method of invariant imbedding (often called the Riccati method, see Refs. [16, 17]) has been used for this purpose, as it is especially suited for parameter scans [11].
Since this method can be used to solve any system of ordinary differential equations, consider for the moment a general linear system

$$\chi_1' = A\chi_1 + B\chi_2 \qquad \chi_2' = C\chi_1 + D\chi_2, \tag{18}$$

where it is shown below how the matrices A, B, C and D and the vectors χ_1 and χ_2 are related to the M_i and $\mathbf{\Phi}$ of the original system given by Eq. (17).
In the Riccati method the vectors χ_1 and χ_2 are linked by the so-called Riccati matrix R via

$$\chi_1 = R\chi_2. \tag{19}$$

From Eqs. (18) and (19) it is possible to infer a matrix differential equation (Riccati equation)

$$R' = AR + B - RCR - D \tag{20}$$

for R [16], which is to be solved instead of the original system. The Riccati equation is integrated from both end points of the interval $[0, a]$ (a is the minor radius of the toroidal device.) simultaneously towards an arbitrarily chosen fit point ξ at which R equals R_{left} and R_{right}, respectively [11, 16]. The eigenvalue is found by iterating ω until $\det\left(R_{\mathrm{left}} - R_{\mathrm{right}}\right) = 0$ holds at the fit point. The code uses a complex secant method to find the roots of the determinant and an accurate integration scheme with adaptive step size for the integration of Eq. (20).
The eigenfunctions are computed using Eq. (19) once ω and therefore also $R(\omega, r)$ have been found. The initial value for χ_2 at ξ comes from a singular value decomposition of $R_{\mathrm{left}} - R_{\mathrm{right}}$ [11].

B. Boundary conditions

By employing the Riccati scheme, the boundary conditions of the physical problem are transformed into initial conditions for R [16]. The initial conditions are always chosen as $R(0) = R(a) = 0$, which can via Eq. (19) be translated to $\chi_1(0) = \chi_1(a) = \mathbf{0}$. Which physical boundary conditions are realized therefore depends on the definition of χ_1 and χ_2.
For the fourth-order system, the physically correct boundary conditions are given as

$$\begin{aligned} \mathbf{\Phi}(0) &= \mathbf{0}, \quad \mathbf{\Phi}(a) = \mathbf{0} \\ \mathbf{\Phi}''(0) &= \mathbf{0}, \quad \boldsymbol{E}_{\parallel}(a) = \mathbf{0}, \end{aligned} \tag{21}$$

if an ideally conducting wall surrounds the plasma. But since it is difficult to access the parallel electric field directly in the code the condition $\mathbf{\Phi}''(a) = \mathbf{0}$ is chosen instead of $\boldsymbol{E}_{\parallel}(a) = \mathbf{0}$ (making the boundary conditions symmetric). According to Ref. [18] the parallel electric field can be approximated by

$$E_{\parallel} \cong -\mathrm{i}\rho_{\mathrm{s}}^2 \left(1 - \mathrm{i}\delta\right) k_{m,n} \left(\nabla \cdot \nabla_{\perp}\right) \Phi, \tag{22}$$

where $\delta \ll 1$ is related to the imaginary part of d_{rad} given in Eq. (14). Taking into account that

$$\nabla \cdot \nabla_{\perp} = \delta_0 \left[1 + \sum_{\mu,\nu} \epsilon_{\mathrm{g}}^{(\mu,\nu)} \cos\left(\mu\Theta - \nu N_{\mathrm{P}} \varphi\right)\right] \frac{\partial^2}{\partial r^2} + \frac{\delta_0}{r^2} \frac{\partial^2}{\partial \Theta^2} \tag{23}$$

for the stellarator it can easily be verified that choosing $\Phi(a) = \Phi''(a) = 0$ indeed ensures $E_{\parallel}(a) = 0$ and that there is no conflict of boundary conditions. Generally, the conditions at $r = a$ are 'real' boundary conditions determined by the nature of the plasma boundary, whereas the conditions at $r = 0$ are regularity conditions. They ensure a finite amplitude of the solution at the origin and are valid for $|m| > 0$.
Thus, it is feasible to define

$$\chi_1 = \left(\mathbf{\Phi}, \mathbf{\Phi}''\right)^{\mathrm{T}} \qquad \text{and} \qquad \chi_2 = \left(\mathbf{\Phi}', \mathbf{\Phi}'''\right)^{\mathrm{T}} \tag{24}$$

making it staightforward to find expressions for the matrices A, B, C and D in terms of the M_i. These calculations yield

$$\begin{aligned} A &= \begin{pmatrix} \underline{0} & \underline{0} \\ \underline{0} & \underline{0} \end{pmatrix} & B &= \begin{pmatrix} \underline{1} & \underline{0} \\ \underline{0} & \underline{1} \end{pmatrix} \\ C &= \begin{pmatrix} \underline{0} & \underline{1} \\ -M_4^{-1} M_0 & -M_4^{-1} M_2 \end{pmatrix} & D &= \begin{pmatrix} \underline{0} & \underline{0} \\ -M_4^{-1} M_1 & -M_4^{-1} M_3 \end{pmatrix}, \end{aligned} \tag{25}$$

where $\underline{0}$ und $\underline{1}$ denote the zero and unity matrix of size $\Delta m \times \Delta m$ respectively.

IV. BENCHMARKS

STAE-K with its simplified physical model is primarily intended to be a reliable tool to quickly scan a certain region in parameter space for interesting fast-particle physics. The same region can then be investigated with more advanced gyrokinetic codes (such as GYGLES [19–21] or EUTERPE) to check whether the prediction from the simplified model holds. Note that these more advanced codes require much more time for their simulations than STAE-K. However, it must be checked that STAE-K calculates the correct results within its range of validity. To this end, several benchmarks have been performed.

A. ITPA benchmark

The ITPA benchmark [22] is one of the most rigorous benchmarks that have been performed of codes calculating fast-ion-driven instabilities. It consists of a rather idealized

scenario, which involves only two modes with poloidal and toroidal mode numbers $m_1 = 10, n_1 = 6$ and $m_2 = 11, n_2 = 6$. They form a gap in the Alfvén continuum at exactly $r/a = 0.5$ as can be seen in Fig. 1. In this scenario, a large-aspect-ratio tokamak with circular flux surfaces is used. The background-plasma parameters are listed in Tab. I (see Appendix B). Note that the bulk plasma is treated within an ideal and reduced MHD framework with negligible plasma beta. This means that pressure terms and consequently any term including a finite bulk-plasma temperature have been left out. For simplicity, the background-plasma density as well as the fast-particle temperature profile are chosen to be flat. Hence, the only free energy source to drive the TAE unstable is the fast-particle density gradient. The fast-particle parameters can be found in Tab. II. The energetic particles possess a Maxwellian equilibrium distribution function.

Starting with the real eigenfrequency of an ideal-MHD calculation, fast particles with increasing temperature are added. As the energetic-particle density profile has its maximum gradient in the region where the mode is localized, energy transfer from the fast particles to the mode by means of inverse Landau damping is possible, driving the mode unstable. The results of this benchmark can be seen in Fig. 2, where STAE-K is compared with various other codes. CAS3D-K [23] is an eigenvalue code which relies on a model of ideal MHD for the background plasma and, similarly to STAE-K, treats the fast particles kinetically. However, CAS3D-K is a perturbative code, whereas STAE-K is non-perturbative. Although differing in details, the two codes possess enough analogies that it is possible to expect a good agreement between them, at least for low enough temperatures, where the perturbative approach of CAS3D-K is valid. CKA-EUTERPE [24] and GYGLES are both particle-in-cell (PIC) codes, but while GYGLES is fully kinetic, CKA-EUTERPE employs an MHD-kinetic hybrid model.

In Fig. 2 one can see that all codes predict a strong increase in the growth rate γ for temperatures up to $T_{\text{fast}} \cong 200$ keV. For higher temperatures, finite-orbit-width (FOW) effects lead to a saturation of γ for CKA-EUTERPE and GYGLES. If finite-Larmor-radius (FLR) effects are excluded in the GYGLES calculation, it agrees up to larger T_{fast} with the result obtained by STAE-K. The reason is that FOW- and FLR effects introduce an averaging effect over the perturbed potential [24, 25]. This means that the effective particle-wave energy transfer is smaller, leading to a reduced growth rate. As expected, the quantitative agreement between CAS3D-K and STAE-K (both codes neglect FOW- and FLR effects) is good in the zero to 200 keV interval, and they qualitatively agree in predicting a strong growth rate for higher fast-ion temperatures.

In this benchmark not only the growth rate, but also the change in the real frequency due to the presence of energetic particles has been calculated. The results are shown in Fig. 3 where the same codes (with the same colours) have been compared as in Fig. 2. As before, STAE-K and CAS3D-K show the best agreement for low enough temperatures, which is to be expected due to the similarities in their mathematical models. The result from GYGLES shows a different behaviour because of its higher level of complexity. Please note that an initial-value approach like the PIC method converges to the fastest growing mode, which is not necessarily identical to the initial MHD eigenmode. STAE-K on the other hand is able to track the development of the same mode during a parameter scan.

On the left-hand side of Fig. 3 it is shown how the mode frequency decreases rapidly with increasing T_{fast} and thus quickly escapes from the MHD continuum gap. As soon as the mode frequency intersects the continuum, continuum damping sets in and the eigenfunctions develop singularities. Since these singularities in position space can be treated in formal analogy to the singularities in velocity space present in conventional Landau damping, the path of integration was extended into the complex plane [11]. The diagram on the left-hand side of Fig. 3 is inspired by the figures in Ref. [21], from where the results of GYGLES have been taken. As the mode frequency always stays inside the continuum gap for this curve, such a representation next to the MHD continuum is valid. The right-hand side of Fig. 3 shows the same results from the codes, but this time together with the kinetic continuum. (The reader is refered to Sec. V A and Fig. 8 for more details on the calculation of the continuum.) In contrast to the MHD continuum, the kinetic continuum changes with T_{fast}. For low T_{fast} it moves together with the mode frequency. At larger temperatures however, the gap gets narrower and the mode again leaves the continuum gap and becomes singular.
From both diagrams of Fig. 3 and also from Fig. 2, the validity range of STAE-K can be estimated. For the conditions of the ITPA benchmark, the code is able to calculate the correct results for fast-particle temperatures $T_{\text{fast}} \lesssim 200$ keV. Progress, in terms of improving the physical model, could be made, if FOW (and as a second step FLR) effects were included. They should bring the γ calculated by STAE-K down to the same range as the results from the PIC codes for higher temperatures. Also, with this first benchmark the numerical feasibility of the Riccati shooting method used to solve the equations has been confirmed. STAE-K is able to calculate the curves in all the figures above in less than half an hour on a single 2.3 GHz core, making STAE-K one to two orders of magnitude faster than the other codes.

B. Benchmark with KIN-2DEM and others

Just like in the ITPA benchmark, this benchmark (refered to as benchmark-1 in Ref. [24] and introduced originally as a benchmark for KIN-2DEM [26]) investigates the change of the real frequency of the mode and the development of the growth rate γ for different fast-particle temperatures. In this case however, the fast-particle beta (using the usual symbols)

$$\beta_{\text{fast},0} = \frac{2\mu_0 k_{\text{B}} N_{\text{fast},0} T_{\text{fast},0}}{B_0^2} \tag{26}$$

on the magnetic axis will be held fixed by keeping $N_{\text{fast},0} T_{\text{fast},0} = 7.578 \cdot 10^{20}$ keV $\cdot$ m^{-3} constant. The two modes ($m_1 = 2, n_1 = 2$ and $m_2 = 3, n_2 = 2$) considered in this tokamak scenario form an MHD continuum that can be seen in Fig. 4. The background-plasma density profile and the fast-particle temperature profile are again chosen to be flat, so that the drive of the mode only arises from the density gradient of the fast particles. All other bulk-plasma parameters are listed in Tab. III, and the remaining parameters of the energetic particles, having a Maxwellian equilibrium distribution function, can be found in Tab. IV.
The growth rate calculated by all the different codes is depicted in Fig. 5. As the fast-

particle beta is kept constant here, the growth rate increases much more slowly with increasing T_{fast} than for the ITPA benchmark. One can see that all MHD-kinetic hybrid codes (STAE-K, CAS3D-K, and NOVA-K) predict nearly the same result. In its general behaviour STAE-K is closest to NOVA-K. Note that for this comparison an older version of NOVA-K [25, 27], which does not include FOW- and FLR effects, was used, which makes the underlying physical model very similar to that of STAE-K. Just like STAE-K, LIGKA [28] is a non-perturbative eigenvalue code but with a much more complex model, and it is not surprising that these two codes show differences.
It can also be noted that for fast-ion velocities less than approximately $v_{\text{A},0}/2$, the mode is still damped. All the codes agree very well in determining the location of the marginal point where the growth rate becomes zero. The existence of such a marginal point can be understood from Eq. (10). At the marginal point, the condition $m\omega_\star = \omega$ is fulfilled, making $h_m^{(1)}$ exactly zero. Thus, there is no contribution of the energetic particles to the perturbed electric current density $\mathbf{j}^{(1)}$ in the plasma, and γ thus vanishes. In order to allow for a non-vanishing growth rate, the diamagnetic drift frequency of the energetic particles (multiplied by m) must exceed the mode frequency. As $\omega_\star$ is given by

$$\omega_\star = -\frac{k_{\text{B}} T_{\text{fast}} \left(\ln N_{\text{fast}} - \frac{3}{2} \ln T_{\text{fast}}\right)' + \varepsilon \left(\ln T_{\text{fast}}\right)'}{M \Omega_0 r} \tag{27}$$

for a Maxwellian distribution function of the energetic particles, it is possible to increase $\omega_\star$ by having steeper gradients in both the density and temperature profile, or by having a higher fast-particle energy ε if the temperature profile is not flat.
For the purpose of this benchmark, radiative damping and electron Landau damping have not been taken into account as they would modify the position of the marginal point and the total growth rate. The change of the real frequency, $\delta\omega = \text{Re}(\omega) - \omega_{\text{MHD}}$, is shown in Fig. 6. All codes show good qualitative agreement. As for the ITPA benchmark, the mode frequency decreases rapidly in the beginning and it increases again with rising fast-particle temperature.

C. Landau damping in the ITPA benchmark

In this benchmark, only the contributions of Landau damping [29] on the modes will be investigated. All gradients are therefore set to zero (corresponding to $\omega_\star \equiv 0$) and thus only kinetic terms that act stabilizing are retained.
In Ref. [30] an analytic formula, capable of making a theoretical prediction about the Landau damping rate of gap modes, has been derived. A very similar equation

$$\delta\omega = -\frac{\beta^\star_{\text{fast}}}{8 k^{\star 2}_{m,n} r^{\star 2}} \omega \frac{r^{\star 2}}{R_0^2} \sum_{j=\pm 1} G\left(x_j\right) \tag{28}$$

with

$$G\left(x_j\right) = 3x_j^2 + 2x_j^4 + x_j \text{Re}\left(Z\left(x_j\right)\right)\left[1 + 2x_j^2 + 2x_j^4\right] \tag{29}$$

and

$$x_j = \frac{\left| q^\star R_0 k^\star_{\parallel,m} \right| v^\star_{\mathrm{A}}}{\left| q^\star R_0 k^\star_{\parallel,m} + j \right| v^\star_{\mathrm{fast}}} \tag{30}$$

can also be found for the change of the real frequency. The superscript * indicates that the quantity in question should be evaluated in the centre of the TAE gap, i.e. where the continua would cross in the cylindrical limit. Hence, Eq. (28) is valid in the limit of very small inverse aspect ratio. Here, this is achieved by choosing a large major radius. The comparison of STAE-K with the analytic theory of Ref. [30] as well as with Eq. (28) is shown in Fig. 7 for the parameters of the ITPA benchmark. While the top diagram shows the normalized damping rate, the normalized deviation from the MHD frequency is depicted in the diagram on the bottom.
It can be observed that, even for small major radii, the qualitative behaviour of the damping rate calculated by STAE-K matches that from analytic theory. If R_0 is increased further, the curves converge to the theoretical result.
In the top diagram of Fig. 7 it can be seen that the damping rate possesses two distinct minima. These correspond to resonances of the fast-particle thermal velocity with respect to the Alfvén velocity [23, 30].

V. RESULTS

A. Changes in the MHD continuum due to energetic-particle influences

STAE-K is not only able to calculate the growth rate, frequency and the structure of the eigenfunction of the mode, but also the shear Alfvén wave continuum. This is done by computing the frequencies for which $\det M_2 = 0$, with M_2 from Eq. (17) in the absence of radiative damping, is satisfied. The continuum of M_2, together with the MHD continuum, is resolved if the fourth-order term is taken into account, which leads to a discretization of the continuum as has been reported in Ref. [6].
Here, the influence of the fast particles on the MHD continuum without radiative damping is studied. The same magnetic geometry as in the ITPA benchmark has been used.
Fig. 8 shows that the continuum can be deformed substantially, if the pressure of the energetic particles becomes comparable to the bulk-plasma pressure. Since both the continuum as well as the discrete TAE frequency within the gap are shifted to lower frequencies, the mode can stay longer inside the gap and is not subject to continuum damping. This maximizes the kinetic drive of the mode. Note that eventually, for $T_{\mathrm{fast}} \gtrsim 300$ keV, the TAE intersects the continuum, so that the TAE transfers energy to singular continuum modes.

B. Contribution of radiative- and background-plasma Landau damping

The singular eigenfunctions resulting from the continuum interaction indicate that the MHD-kinetic hybrid model is not well suited to explain the physics on very short spatial scales. The model can be improved by including kinetic effects of finite Larmor radii of

the background-plasma ions, as well as a kinetically arising parallel electric field. They cause the so-called radiative damping, governed by the fourth-order operator given in Eq. (13) [13].
Since the addition of this term discretizes the MHD continuum (including also the fast-particle influences), it resolves any continuum interaction as can be seen in Fig. 9 for the parameters of the ITPA benchmark. A constant bulk-plasma temperature of 1 keV was chosen. The eigenfunctions show no singularities indicative of continuum damping. Instead, the figure shows the smooth transition of a TAE into a a kinetically modified TAE (KTAE) and later into a kinetic Alfvén wave (KAW). Short-scale oscillations start to appear on the mode structure precisely when the fast-particle temperature is such that the mode would intersect the Alfvén continuum, if radiative damping were not present. The oscillations are only present in the real and imaginary part (not shown in the figure) of the eigenfunction. They are absent in the absolute value of the potential perturbation, which thus resembles the results of Ref. [21] very closely. Note that no short-scale oscillations in the eigenfunction are observed in Ref. [21]. We conjecture that they are an effect of the much larger growth rate of this model due to the absence of FOW- and FLR effects. Additionally, the mode frequency in Ref. [21] never intersects the continuum, which is found to be an essential condition for the appearance of oscillations.
The final mode structure is broader, shifted towards the position of the maximal gradient in N_{fast}, and one poloidal harmonic dominates over the others. All these are signs for EPMs [21].
The model includes the kinetic drive of the energetic particles as well as damping mechanisms such as Landau damping (of both the bulk ions and electrons), radiative damping, and, if the continuum gap is closed, continuum damping. In order to assess the overall stability of a mode, damping is just as important as the drive. For the ITPA case introduced above, calculations have also been performed without fast particles. The combined damping rate of radiative damping and Landau damping of the background-plasma electrons was $\gamma = -2.33 \cdot 10^3\ \text{s}^{-1}$, which is very close to results from more advanced codes like LIGKA and GYGLES giving $\gamma = -2.34 \cdot 10^3\ \text{s}^{-1}$ and $\gamma = -3.9 \cdot 10^3\ \text{s}^{-1}$, respectively [22].

C. Stability diagrams

The properties of the damping terms are mainly determined by the background plasma, making it feasible to vary fast-particle parameters and background-plasma parameters independently. In doing so, it is possible to scan a whole region in parameter space and to answer the question whether the mode is stable or unstable in this region.
Such stability scans have been performed for the ITPA benchmark case and for a W7-X scenario (introduced below). The bulk and the energetic-particle temperature have been varied independently (N_{fast} and N_{bulk} were kept constant.) to obtain the two stability diagrams shown in Fig. 10 (ITPA benchmark on the left and W7-X on the right). Both calculations include the kinetic drive coming from the fast-particle species as well as Landau damping of the bulk electrons and radiative damping. For both cases radiative damping is able to extend the region of stability, but for high energetic-particle temperatures the drive still dominates. Note that, as a first step, only the toroidal coupling has

been taken into account for W7-X.
The stability scans are performed by repeatedly solving the eigenvalue problem in the plane spanned by T_{fast} and T_{bulk}. As such, computation of the scans parallelizes perfectly. Depending on whether radiative damping was included, these calculations typically take three to ten hours on 128 processors for a resolution of about 256 points in each direction.

D. Application to W7-X

The code will be be applied to the stellarator W7-X in more detail. The background-plasma and fast-particle parameters for the W7-X case are summarized in Tabs. V and VI, respectively, and they lead to an MHD continuum shown in Fig. 11.
As a first step, the influence of a rising energetic-particle temperature on the structure of the eigenfunction is studied. Note that the radiative damping term, with a background temperature of $T_{\text{bulk}} = 1$ keV, has been present in all the calculations in this section. The results can be seen in Fig. 12, where the kinetic continuum and the eigenfunction for a high fast-particle temperature of 750 keV are shown. The kinetic continuum exhibits only minor differences compared with the ideal-MHD continuum. Furthermore, these changes are located at radial positions where the mode amplitude is almost vanishing. Consequently, the influence of the fast particles on the structure of the eigenfunction is negligible. It must also be pointed out that $T_{\text{fast}} = 750$ keV will most likely not be reached in W7-X. The specific case that has been chosen for this investigation is very insensitive to an increasing T_{fast}.
The fast-particle pressure can also be raised by increasing the fast-particle density. The eigenfunction depicted in Fig. 13 again shows no significant deviation from its ideal-MHD counterpart. As previously, this is due to the fact that the continuum only changes in the center and at the edge and that therefore the nature of the coupling between the poloidal harmonics remains unaffected.
Generally, the transition of the TAE into a KTAE happens because the mode frequency gets close to the continuum and because the radiative damping term is present. For the two previous cases with increasing T_{fast} and N_{fast} the mode frequency was nearly unaffected by the fast-particle population. Furthermore, the continuum only changed in regions where the mode was not localized. Thus, no transition into a KTAE could be observed. However, the influence of radiative damping on the structure of the eigenfunction can also be studied in the absence of fast particles by simply modifying the density profile of the background plasma in such a way that the TAE gap closes. Then a combined damping rate of continuum damping and radiative damping is calculated. The density profile was chosen as

$$n_{\text{bulk}}^{\text{profile}} = \frac{1}{2}\left[1 - \tanh\left(\frac{s_h - r}{0.1a}\right)\right] \tag{31}$$

with a shift parameter s_h. It represents the extreme case of a hollow density profile, where at $r = s_h$ the density has increased to half the value at the edge. Here, it is shown as a proof of principle how radiative damping influences the case of extreme continuum

damping. The results of this investigation, together with the different continua for various values of s_h are depicted in Fig. 14. Even though the continuum closes in a region where the mode has a finite amplitude, no singular eigenfunctions are observed. They are instead completely regularized by the presence of the fourth-order damping operator. Now, short-scale oscillations (less prominent than in Fig. 9) develop in the eigenfunctions, and the amplitude of one poloidal harmonic becomes much larger than that of the other one. This investigation without fast particles shows that such behaviour must not necessarily be interpreted as sign of an EPM. It is merely a consequence of the TAE frequency leaving the continuum gap towards a region where mode coupling becomes less important. However, as can be concluded from the ITPA-case, energetic particles can have a similar influence on the mode frequency and the continuum. These results are in qualitative agreement with Ref. [31]. For the extreme case of $s_h = 0.3$ m a damping rate of $(\gamma_{\text{continuum}} + \gamma_{\text{radiative}})/\omega_{\text{MHD}} = -2.32\%$ is measured, where the majority comes from continuum damping as can be observed in Fig. 15. Radiative damping alone accounts for approximately -0.12%.
The figure shows a strong increase of the damping rate $\gamma_{\text{continuum}}$ for $s_h \gtrsim 0.225$ m when just the MHD terms are present. The path of integration has been extended into the complex plane to retain the contribution of the pole. Note that in this logarithmic plot the initial level of $\gamma_{\text{continuum}}$ for small values of s_h is not exactly zero only because of the numerically specified tolerance for convergence. In this initial phase radiative damping outweighs continuum damping by many orders of magnitude. At some point, however, continuum damping also sets in when the fourth-order term is taken into account. In this case it was not necessary to leave the real axis when integrating Eq. (20). As expected, there still are some slight differences in both curves of Fig. 15 for $s_h = 0.3$ m, but they seem to converge to the same damping rate in the limit of very strong damping.

VI. SUMMARY AND CONCLUSIONS

In this paper, the resonant interaction of fast particles with shear Alfvén waves, especially TAEs, leading to EPMs has been investigated in tokamaks and stellarators. The non-perturbative model used for this purpose treats the background plasma within ideal MHD-theory and the fast particles kinetically. Furthermore, a higher-order differential operator, which describes radiative damping, has been added to the model. (To the best knowledge of the authors, this is the first time that radiative damping has been adressed in stellarators.) Throughout this work, the large-aspect-ratio and low-plasma-beta approximations have been used.
The eigenvalue problem is solved by the novel code STAE-K, using a numerically robust and efficient shooting algorithm. Thanks to its high speed, the code is particularly well suited to perform parameter scans in the EPM regime. After a scan has been conducted, specific regions in parameter space can be investigated by more advanced codes with physically more complex models. It can then be checked if the predictions from the simplified model utilized by STAE-K hold.
The behaviour of the shear Alfvén wave continuum in the presence of energetic particles was studied. It was found that the structure of the continuum may be influenced sub-

stantially. In particular, continuum resonances in regions where the mode has a finite amplitude become possible. In this case, continuum damping occurs and the TAE may smoothly be converted into a KAW, if radiative damping is accounted for.
Especially in the W7-X case, it could be observed that the structure of the MHD-eigenfunction is insensitive to changes of T_{fast} and N_{fast}. Thus, perturbative hybrid models like CAS3D-K and CKA-EUTERPE might be applicable for a wide range of fast-particle parameters.
All the W7-X results were obtained taking into account the toroidal coupling only. However, the structure of the magnetic field in W7-X is such that the helical coupling could be of equal importance. More couplings, leading to more realistic results, will be included in the future.
The ITPA benchmark showed that FOW effects play a critical role in determining the growth rate of the mode. A next step will be to properly include those effects into STAE-K. At the same time it must be emphasized again that all results were obtained for a Maxwellian equilibrium distribution function of the energetic particles. Since most circulating fast particles are produced by neutral beam injection, it would be more appropriate to work with a pitch-angle dependent slowing-down distribution function. This topic is left for future work.

Acknowledgment

This work has been carried out within the framework of the EUROfusion Consortium and has received funding from the Euratom research and training programme 2014-2018 under grant agreement No 633053. The views and opinions expressed herein do not necessarily reflect those of the European Commission.

Figures

Figure 1:

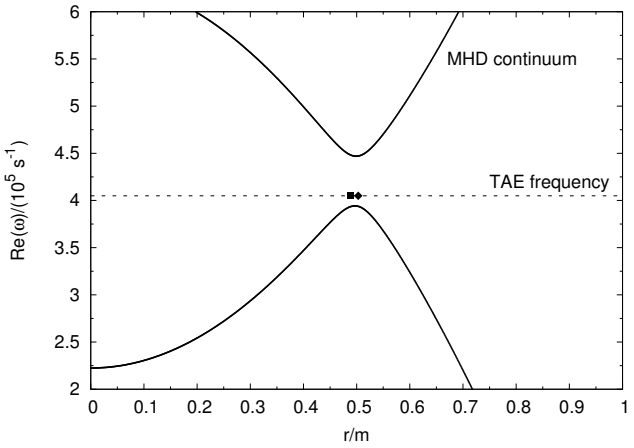

Figure 1: The Alfvén continuum without fast particles for the ITPA benchmark as calculated by STAE-K. The TAE frequency (dashed line) lies in the continuum gap. The locations of the maxima of both eigenmode components Φ_m and Φ_{m+1} have been indicated by a square and a diamond respectively.

Figure 2:

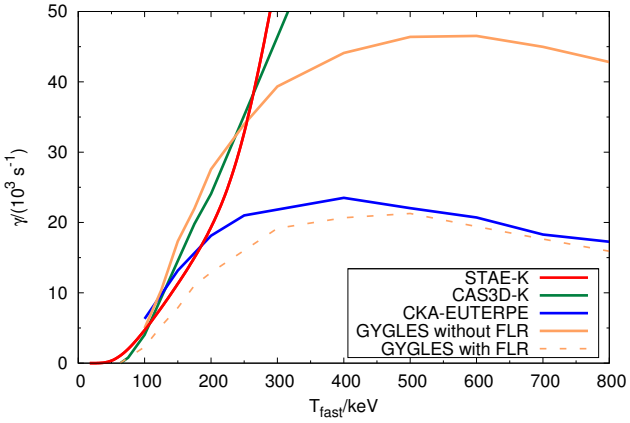

Figure 2: Calculated growth rates of the TAE as a function of the fast-particle temperature within the ITPA framework. All the codes that exclude FOW- (and FLR-) effects show qualitatively the same strong increase in the growth rate. If those effects are taken into account they substantially decrease the growth rate. Curves other than STAE-K taken from [22, 24].

Figure 3:

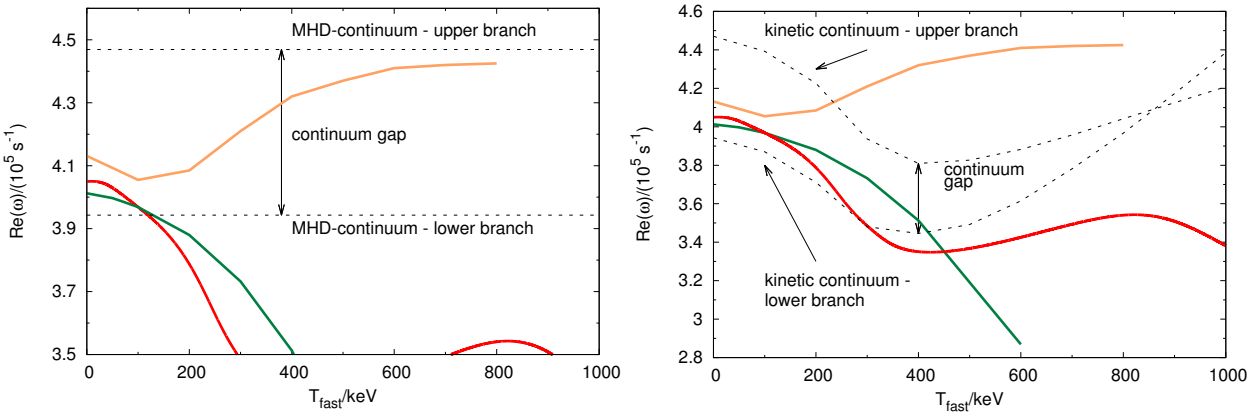

Figure 3: Real part of the TAE frequency as a function of the fast-particle temperature within the ITPA framework. (The colours are the same as in Fig. 2.) Left: Since the frequency is initially decreasing rapidly with increasing fast-ion temperature, the mode quickly leaves the MHD continuum gap. Right: Even though the frequency varies rapidly, the kinetic continuum mimics this behaviour so that the mode frequency remains longer inside the gap. For higher fast-particle temperatures the mode sinks deeply into the continuum. GYGLES curve taken from [21].

Figure 4:

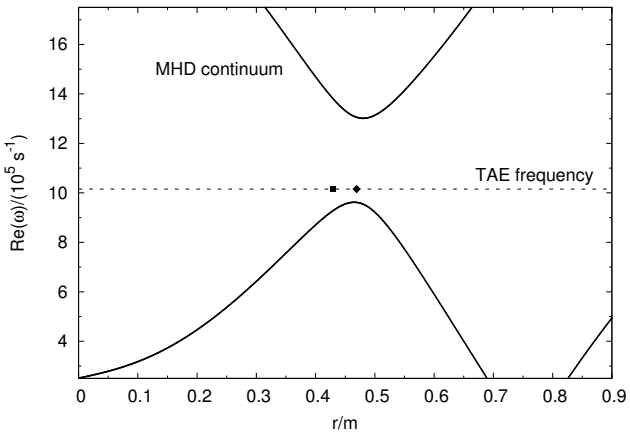

Figure 4: The Alfvén continuum without fast particles for the benchmark with KIN-2DEM and others as calculated by STAE-K. The TAE frequency (dashed line) lies in the continuum gap. The locations of the maxima of both eigenmode components Φ_m and Φ_{m+1} have been indicated by a square and a diamond respectively.

Figure 5:

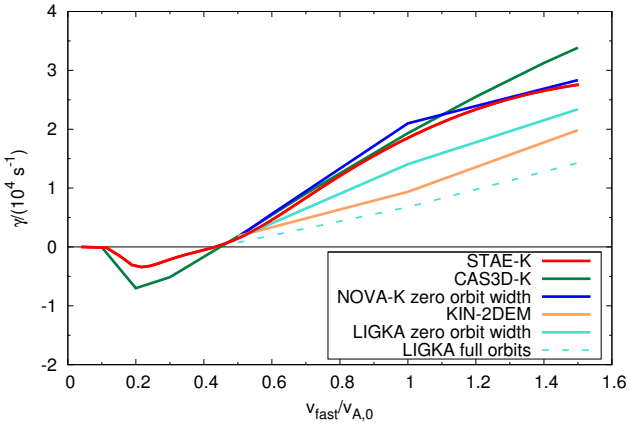

Figure 5: Calculated growth rate of the TAE as a function of the fast-particle thermal velocity normalized to the on-axis Alfvén velocity. All the codes agree in their qualitative behaviour, and STAE-K especially matches the results of other hybrid codes (such as NOVA-K). The marginal point $\gamma = 0$ is the same for all codes. Curves other than STAE-K taken from [26, 28].

Figure 6:

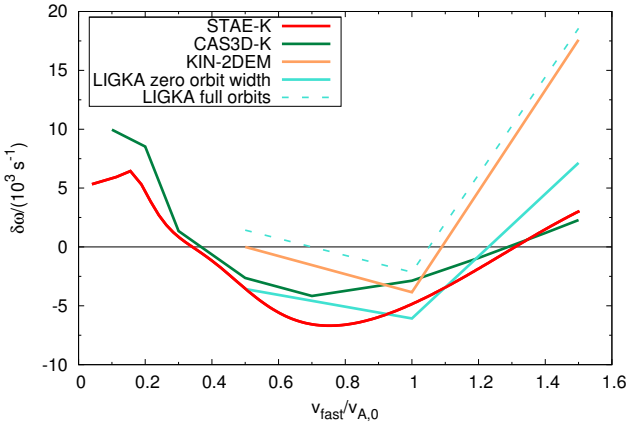

Figure 6: Calculated real part of the TAE frequency as a function of the fast-particle thermal velocity normalized to the on-axis Alfvén velocity. Again STAE-K is close to other hybrid codes (especially CAS3D-K) in this case. The fully kinetic codes predict a much stronger frequency change for high temperatures. Curves other than STAE-K taken from [26, 28].

Figure 7:

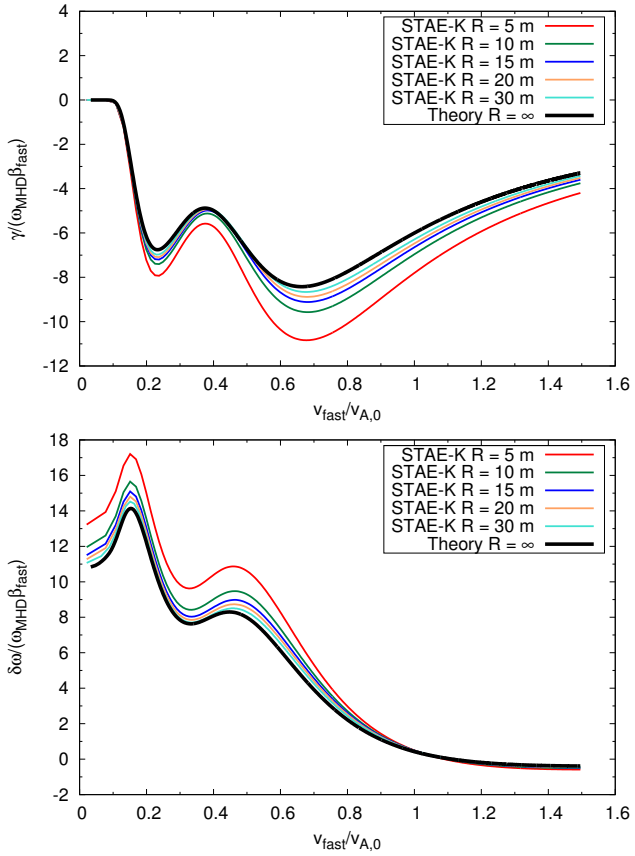

Figure 7: Comparison of STAE-K to analytic theory in the limit of very small inverse aspect ratio for various fast-particle temperatures. Normalized Landau damping rate (top) and normalized change of the real frequency (bottom) as functions of the energetic-particle thermal velocity. STAE-K converges to the theoretical result (black curve) for increasing major radii.

Figure 8:

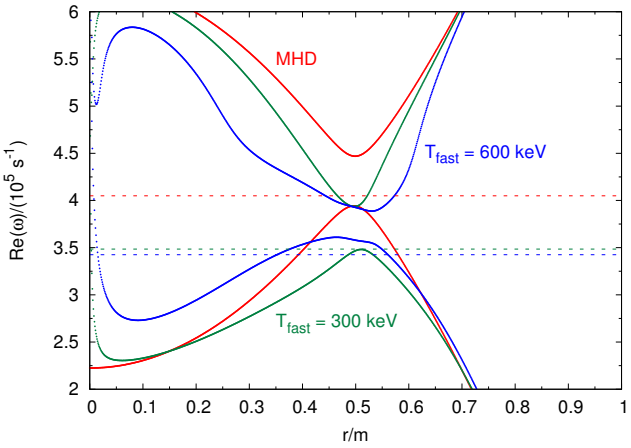

Figure 8: Evolution of the shear Alfvén continuum with increasing temperature of the energetic particles for the parameters of the ITPA benchmark (see Tabs. I and II). The TAE gap as well as the discrete eigenfrequency (dashed lines) are shifted to lower values. For $T_{\text{fast}} \gtrsim 300$ keV the mode frequency intersects the continuum, leading to continuum damping.

Figure 9:

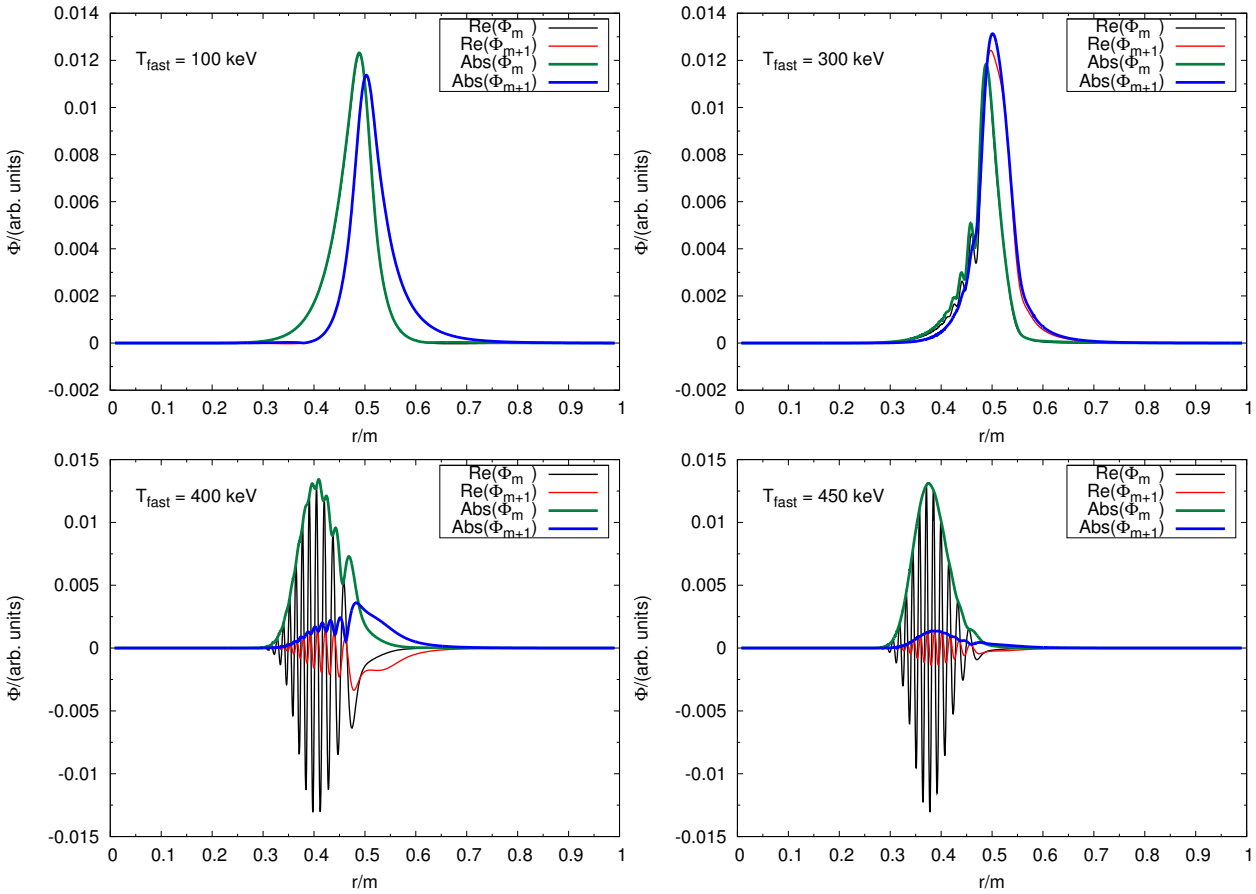

Figure 9: Development of the eigenfunctions in the ITPA case including radiative damping. The mode transforms from a TAE into a KTAE and later into a KAW. Black and red curves show the real parts of both eigenmode components, whereas green and blue have been used for the absolute values.

Figure 10:

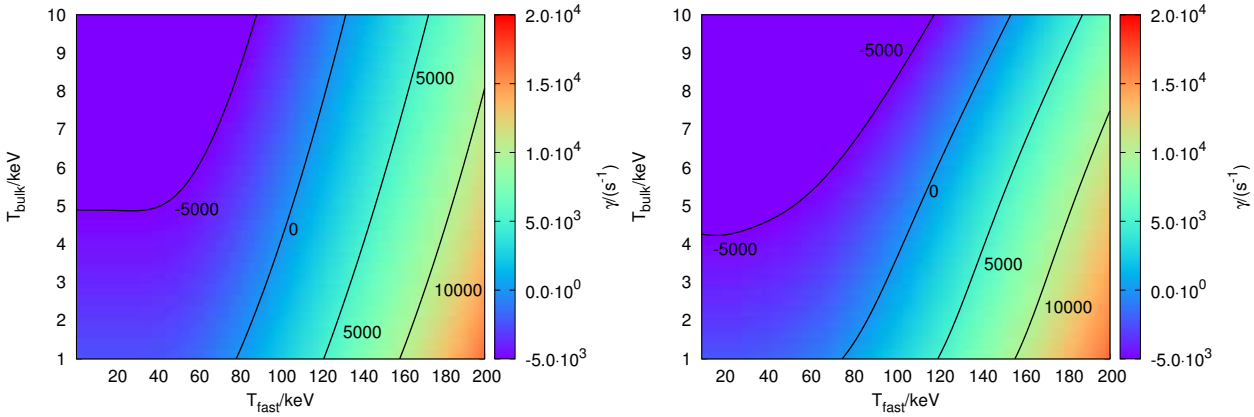

Figure 10: Stability diagrams taking into account the kinetic drive of a fast-particle species, Landau damping by the background-plasma electrons, and radiative damping. Black lines connect points of equal growth/damping rate. Left: ITPA benchmark. Right: W7-X case.

Figure 11:

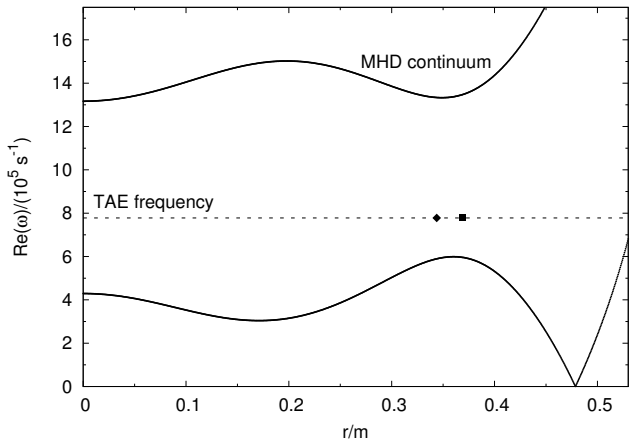

Figure 11: The Alfvén continuum without fast particles for the W7-X case as calculated by STAE-K. The TAE frequency (dashed line) lies in the continuum gap. The locations of the maxima of both eigenmode components $\Phi_{m,n}$ and $\Phi_{m+1,n}$ have been indicated by a square and a diamond respectively.

Figure 12:

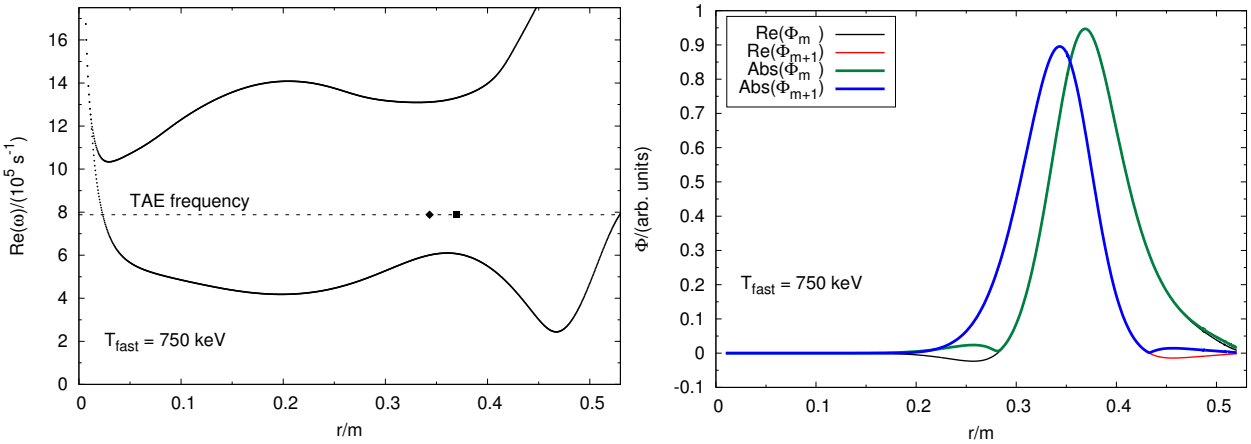

Figure 12: Kinetic continuum (left) and eigenfunction (right) for the W7-X case in the presence of energetic particles with high T_{fast} of 750 keV. The fast-particle density is $N_{\text{fast}} = 4.0 \cdot 10^{17}$ m^{-3}. The eigenfunction is nearly unchanged compared with the ideal-MHD case.

Figure 13:

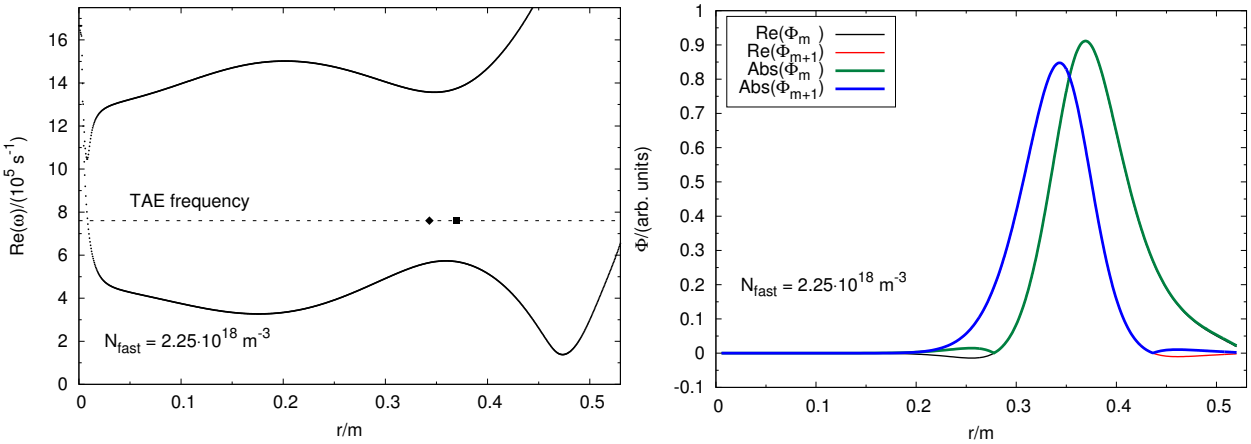

Figure 13: Kinetic continuum (left) and eigenfunction (right) for the W7-X case in the presence of energetic particles with a high ratio of $N_{\text{fast}}/N_{\text{bulk}} = 11.25\%$. The fast-particle temperature is $T_{\text{fast}} = 100$ keV. The eigenfunction is nearly unchanged compared with the ideal-MHD case.

Figure 14:

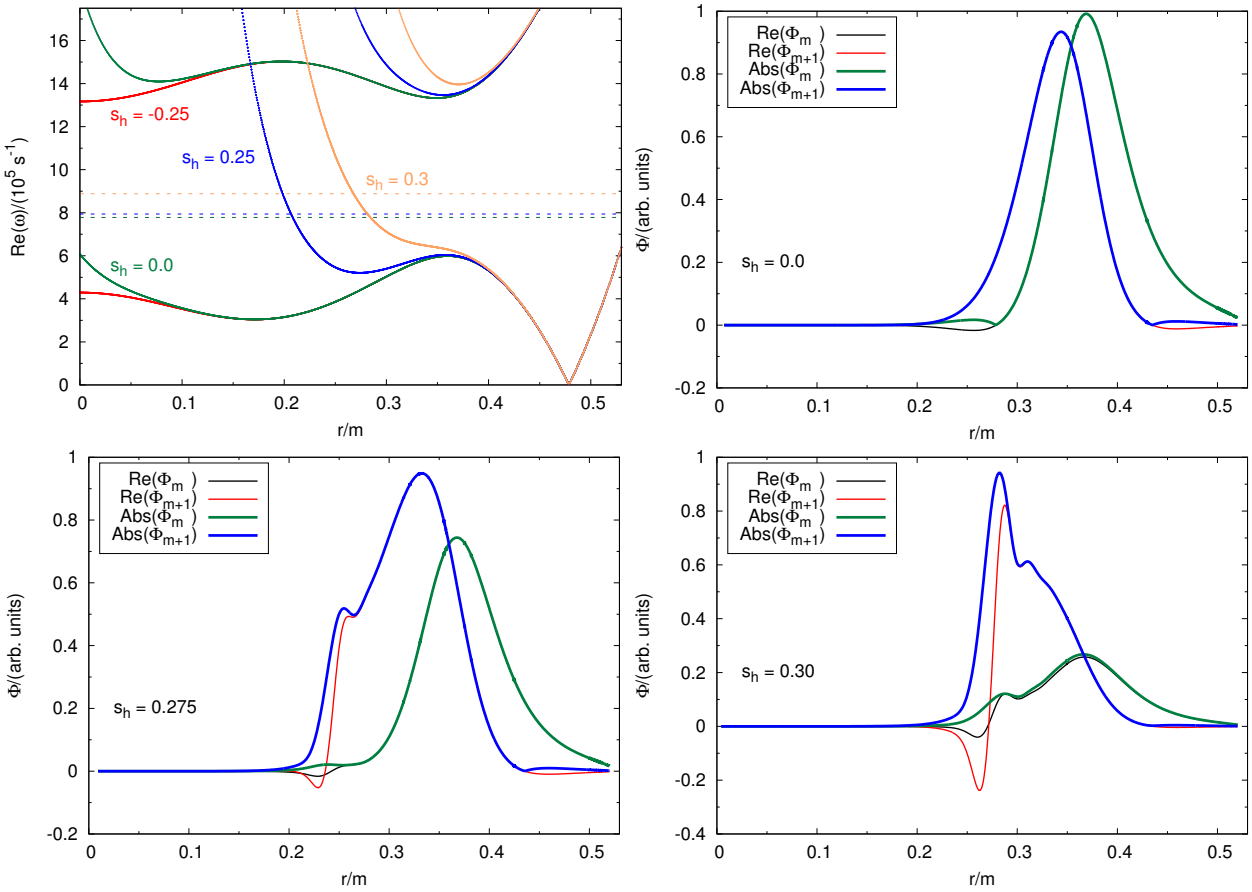

Figure 14: Influence of the radiative damping term on the eigenfunctions for a closing TAE gap (see top left). The eigenfunctions for values of $s_h = 0.0$ (top right), $s_h = 0.275$ (bottom left), and $s_h = 0.3$ (bottom right) are shown. The fourth-order term prevents the development of singularities. No fast particles are present in this calculation.

Figure 15:

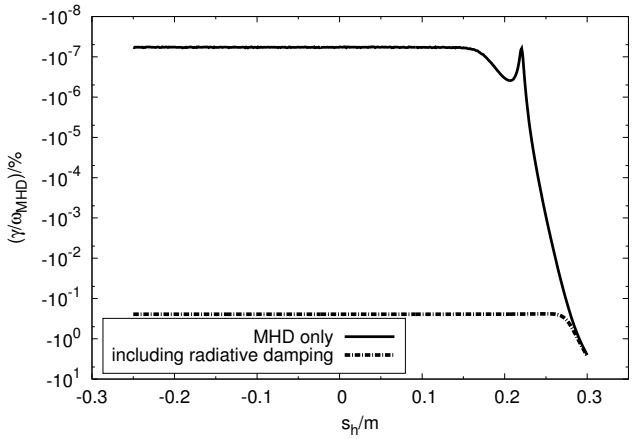

Figure 15: Normalized continuum damping rate only taking into account the MHD terms (full curve) and a combination of radiative damping and continuum damping (dashed line). The shift parameter s_h used to control the density profile determines the strength of the damping.

Appendix A: Fast-particle contribution in detail

Using Eqs. (9) and (12), the Fourier transformed fast-particle contribution to Eq. (1) is obtained as

$$\begin{aligned}\mathcal{FT}\left(\frac{\mathrm{i}\omega\mu_0 r^2}{\alpha^2\delta_0}\nabla\cdot\mathbf{j}^{(1)}_{\mathrm{fast}}\right)\cong\frac{\omega\mu_0 Z_{\mathrm{fast}}\mathrm{e}R_0^2\delta_0}{4}\times\\ \times\left(A_{m,n}\Phi^{(1)}_{m,n}+B_{m+2\sigma,n+2\tau N_{\mathrm{P}}}\Phi^{(1)}_{m+2\sigma,n+2\tau N_{\mathrm{P}}}+C_{m-2\sigma,n-2\tau N_{\mathrm{P}}}\Phi^{(1)}_{m-2\sigma,n-2\tau N_{\mathrm{P}}}\right)\end{aligned} \tag{A1}$$

with

$$\begin{aligned}A_{m,n}=&\left\{\eta_{\sigma,0}\sigma\left(\epsilon_{\mathrm{B}}^{(\sigma,\tau)}\right)^2\left[-\mathcal{C}\left(z_+\right)-\mathcal{C}\left(z_-\right)\right]\right\}\frac{\mathrm{d}^2}{\mathrm{d}r^2}+\\ &+\left\{\eta_{\sigma,0}\epsilon_{\mathrm{B}}^{(\sigma,\tau)}\epsilon_{\mathrm{B}}^{(\sigma,\tau)'}\left[-\mathcal{A}\left(z_+\right)+\mathcal{A}\left(z_-\right)\right]+\right.\\ &\quad+\eta_{\sigma,0}\sigma\left(\epsilon_{\mathrm{B}}^{(\sigma,\tau)}\right)^2\left[-\mathcal{B}\left(z_+\right)-\mathcal{B}\left(z_-\right)\right]+\\ &\quad\left.+\sigma\epsilon_{\mathrm{B}}^{(\sigma,\tau)}\epsilon_{\mathrm{B}}^{(\sigma,\tau)'}\left[\left(m-\eta_{\sigma,0}\right)\mathcal{C}\left(z_+\right)-\left(m+\eta_{\sigma,0}\right)\mathcal{C}\left(z_-\right)\right]\right\}\frac{\mathrm{d}}{\mathrm{d}r}+\\ &+m\left(\epsilon_{\mathrm{B}}^{(\sigma,\tau)'}\right)^2\left[\mathcal{A}\left(z_+\right)+\mathcal{A}\left(z_-\right)\right]+\\ &+m\sigma\epsilon_{\mathrm{B}}^{(\sigma,\tau)}\epsilon_{\mathrm{B}}^{(\sigma,\tau)'}\left[\mathcal{B}\left(z_+\right)-\mathcal{B}\left(z_-\right)\right]+\\ &+m\sigma\epsilon_{\mathrm{B}}^{(\sigma,\tau)}\epsilon_{\mathrm{B}}^{(\sigma,\tau)''}\left[\mathcal{C}\left(z_+\right)-\mathcal{C}\left(z_-\right)\right]\end{aligned} \tag{A2}$$

and

$$\begin{aligned}B_{m+2\sigma,n+2\tau N_{\mathrm{P}}}=&\left[\eta_{\sigma,0}\sigma\left(\epsilon_{\mathrm{B}}^{(\sigma,\tau)}\right)^2\mathcal{C}\left(z_+\right)\right]\frac{\mathrm{d}^2}{\mathrm{d}r^2}+\\ &+\left[\eta_{\sigma,0}\epsilon_{\mathrm{B}}^{(\sigma,\tau)}\epsilon_{\mathrm{B}}^{(\sigma,\tau)'}\mathcal{A}\left(z_+\right)+\eta_{\sigma,0}\left(\epsilon_{\mathrm{B}}^{(\sigma,\tau)}\right)^2\mathcal{B}\left(z_+\right)+\right.\\ &\quad\left.+\sigma\epsilon_{\mathrm{B}}^{(\sigma,\tau)}\epsilon_{\mathrm{B}}^{(\sigma,\tau)'}\left(m+2\sigma+\eta_{\sigma,0}\right)\mathcal{C}\left(z_+\right)\right]\frac{\mathrm{d}}{\mathrm{d}r}+\\ &+\left(m+2\sigma\right)\left[+\left(\epsilon_{\mathrm{B}}^{(\sigma,\tau)'}\right)^2\mathcal{A}\left(z_+\right)+\sigma\epsilon_{\mathrm{B}}^{(\sigma,\tau)}\epsilon_{\mathrm{B}}^{(\sigma,\tau)'}\mathcal{B}\left(z_+\right)+\right.\\ &\quad\left.+\sigma\epsilon_{\mathrm{B}}^{(\sigma,\tau)}\epsilon_{\mathrm{B}}^{(\sigma,\tau)''}\mathcal{C}\left(z_+\right)\right]\end{aligned} \tag{A3}$$

and

$$
\begin{aligned}
C_{m-2\sigma,n-2\tau N_\mathrm{P}} = &\left[\eta_{\sigma,0}\sigma\left(\epsilon_\mathrm{B}^{(\sigma,\tau)}\right)^2\mathcal{C}\left(z_-\right)\right]\frac{\mathrm{d}^2}{\mathrm{d}r^2}+\\
&+\Bigg[-\eta_{\sigma,0}\epsilon_\mathrm{B}^{(\sigma,\tau)}\epsilon_\mathrm{B}^{(\sigma,\tau)'}\mathcal{A}\left(z_-\right)+\eta_{\sigma,0}\left(\epsilon_\mathrm{B}^{(\sigma,\tau)}\right)^2\mathcal{B}\left(z_-\right)+\\
&\quad-\sigma\epsilon_\mathrm{B}^{(\sigma,\tau)}\epsilon_\mathrm{B}^{(\sigma,\tau)'}\left(m-2\sigma-\eta_{\sigma,0}\right)\mathcal{C}\left(z_-\right)\Bigg]\frac{\mathrm{d}}{\mathrm{d}r}+\\
&+\left(m-2\sigma\right)\Bigg[\left(\epsilon_\mathrm{B}^{(\sigma,\tau)'}\right)^2\mathcal{A}\left(z_-\right)-\sigma\epsilon_\mathrm{B}^{(\sigma,\tau)}\epsilon_\mathrm{B}^{(\sigma,\tau)'}\mathcal{B}\left(z_-\right)+\\
&\quad-\sigma\epsilon_\mathrm{B}^{(\sigma,\tau)}\epsilon_\mathrm{B}^{(\sigma,\tau)''}\mathcal{C}\left(z_-\right)\Bigg].
\end{aligned}
\tag{A4}
$$

Here, σ and τ represent the particular mode coupling, $z_\pm = \left(m \pm \sigma, n \pm \tau N_\mathrm{p}\right)$ and $\eta_{\sigma,0}$ is a 'reversed' Kronecker-delta: $\eta_{\sigma,0} = 1 - \delta_{\sigma,0}$.
The operators $\mathcal{A}, \mathcal{B}$ and $\mathcal{C}$ are defined as

$$
\mathcal{A}\left(\overline{m},\overline{n}\right) = \overline{m}\left(1+\frac{\overline{m}}{\omega}a\right)\mathcal{I}_1\left(\overline{m},\overline{n}\right)+\frac{\overline{m}^2}{\omega}b\mathcal{I}_2\left(\overline{m},\overline{n}\right) \tag{A5}
$$

and

$$
\begin{aligned}
\mathcal{B}\left(\overline{m},\overline{n}\right) = &\left[-\frac{1}{r}\left(1+\frac{\overline{m}}{\omega}a\right)+c\left(1+\frac{\overline{m}}{\omega}a\right)+\frac{\overline{m}}{\omega}\left(d-\frac{a}{r}\right)\right]\mathcal{I}_1\left(\overline{m},\overline{n}\right)+\\
&+\left[-\frac{1}{r}\frac{\overline{m}}{\omega}b+\frac{\overline{m}}{\omega}cb+e\left(1+\frac{\overline{m}}{\omega}a\right)+\frac{\overline{m}}{\omega}\left(f-\frac{b}{r}\right)\right]\mathcal{I}_2\left(\overline{m},\overline{n}\right)+\\
&+\frac{\overline{m}}{R_0}\frac{q'}{q^2}\left(1+\frac{\overline{m}}{\omega}a\right)\mathcal{I}_3\left(\overline{m},\overline{n}\right)+\frac{\overline{m}}{R_0}\frac{q'}{q^2}\frac{\overline{m}}{\omega}b\mathcal{I}_4\left(\overline{m},\overline{n}\right)+\frac{\overline{m}}{\omega}eb\mathcal{I}_5\left(\overline{m},\overline{n}\right)
\end{aligned}
\tag{A6}
$$

and

$$
\mathcal{C}\left(\overline{m},\overline{n}\right) = \frac{\mathcal{A}\left(\overline{m},\overline{n}\right)}{\overline{m}}. \tag{A7}
$$

While the quantities $a, \ldots, f$ contain the density and temperature gradients of the energetic particles

$$
a = \frac{\delta_0^2 k_\mathrm{B}}{M\Omega_0 r}\left[T\left(\ln N\right)' - \frac{3}{2}T'\right] \tag{A8}
$$

$$
b = \frac{\delta_0^2}{M\Omega_0 r}\left(\ln T\right)' \tag{A9}
$$

$$
c = \left(\ln N\right)' - \frac{5}{2}\left(\ln T\right)' \tag{A10}
$$

$$
d = \frac{\delta_0^2 k_\mathrm{B}}{M\Omega_0 r}\left[T'\left(\ln N\right)' + T\left(\ln N\right)'' - \frac{3}{2}T''\right] \tag{A11}
$$

$$
e = \frac{1}{k_\mathrm{B}T}\left(\ln T\right)' \tag{A12}
$$

$$
f = \frac{\delta_0^2}{M\Omega_0 r}\left(\ln T\right)'', \tag{A13}
$$

the different integrals over velocity space are denoted by

$$\mathcal{I}_1\left(\overline{m},\overline{n}\right) = \int \mathrm{d}^3 v \, \frac{v_{\mathrm{D},0}^2}{\omega - v_\parallel k_{\overline{m},\overline{n}}} \frac{\partial F}{\partial \varepsilon} \tag{A14}$$

$$\mathcal{I}_2\left(\overline{m},\overline{n}\right) = \int \mathrm{d}^3 v \, \frac{v_{\mathrm{D},0}^2}{\omega - v_\parallel k_{\overline{m},\overline{n}}} \frac{\partial F}{\partial \varepsilon} \varepsilon \tag{A15}$$

$$\mathcal{I}_3\left(\overline{m},\overline{n}\right) = \int \mathrm{d}^3 v \, \frac{v_{\mathrm{D},0}^2}{\left(\omega - v_\parallel k_{\overline{m},\overline{n}}\right)^2} v_\parallel \frac{\partial F}{\partial \varepsilon} \tag{A16}$$

$$\mathcal{I}_4\left(\overline{m},\overline{n}\right) = \int \mathrm{d}^3 v \, \frac{v_{\mathrm{D},0}^2}{\left(\omega - v_\parallel k_{\overline{m},\overline{n}}\right)^2} v_\parallel \frac{\partial F}{\partial \varepsilon} \varepsilon \tag{A17}$$

$$\mathcal{I}_5\left(\overline{m},\overline{n}\right) = \int \mathrm{d}^3 v \, \frac{v_{\mathrm{D},0}^2}{\omega - v_\parallel k_{\overline{m},\overline{n}}} \frac{\partial F}{\partial \varepsilon} \varepsilon^2. \tag{A18}$$

Note that the equations presented in this appendix are valid for the stellarator. Their tokamak equivalents may be recovered by setting $\sigma = 1, \tau = 0$ (toroidal coupling), $\delta_0 = 1$ (circular flux surfaces), and $\epsilon_{\mathrm{B}}^{(1,0)} = -r/R_0$.

Appendix B: Parameters of the numerical calculations

Below, the parameters which have been used in the various benchmarks and in the W7-X calculation are listed.

Table I: Background-plasma parameters for the ITPA benchmark

Major radius R_0/m	10.0
Minor radius a/m	1.0
Mode numbers (m_1, n_1) and (m_2, n_2)	$(10, 6)$ and $(11, 6)$
Magnetic field B_0/T on axis	3.0
Type of ions	hydrogen
Density $n_{\mathrm{i},0}/\mathrm{m}^{-3}$ on axis	$2.0 \cdot 10^{19}$
Density profile	flat
q-profile	$q(r) = 1.71 + 0.16r^2$

Table II: Fast-particle parameters for the ITPA benchmark

Type of ions	deuterium
Density $N_{\mathrm{fast},0}/\mathrm{m}^{-3}$ on axis	$0.75 \cdot 10^{17}$
Density profile	$N_{\mathrm{fast}}(r) = c_3 \exp\left[-c_2/c_1 \cdot \tanh\left\{(r - c_0)/c_2\right\}\right]$
Coefficients	$c_0 = 0.491, c_1 = 0.298, c_2 = 0.199, c_3 = 0.521$
Temperature $T_{\mathrm{fast},0}/\mathrm{keV}$ on axis	$1 \ldots 800$
Temperature profile	flat

Table III: Background-plasma parameters for the benchmark with KIN-2DEM and others

Major radius R_0/m	4.0
Minor radius a/m	0.9
Mode numbers (m_1, n_1) and (m_2, n_2)	$(2, 2)$ and $(3, 2)$
Magnetic field B_0/T on axis	5.0
Type of ions	deuterium
Density $n_{\mathrm{i},0}/\mathrm{m}^{-3}$ on axis	$5.0 \cdot 10^{19}$
Density profile	flat
q-profile	$q(r) = \sum_{i=0}^{6} c_i r^i$
Coefficients	$c_0 = 1.048, c_1 = 0.101, c_2 = 0.077$ $c_3 = 3.334, c_4 = -6.748, c_5 = 5.965$ $c_6 = -2.024$

Table IV: Fast-particle parameters for the benchmark with KIN-2DEM and others

Type of ions	hydrogen
Density $N_{\text{fast},0}$ on axis	chosen to keep $T_{\text{fast},0}N_{\text{fast},0} \cong 7.6 \cdot 10^{20}$ keV $\cdot$ m^{-3} constant
Density profile	$N_{\text{fast}}(r) = \exp\left[-\left(c_0 + \sqrt{c_1 + c_2 r^2}\right)/c_3\right]$
Coefficients	$c_0 = -1.75, c_1 = 3.063, c_2 = 5.556, c_3 = 0.09$
Temperature $T_{\text{fast},0}$ on axis	chosen to keep $T_{\text{fast},0}N_{\text{fast},0} \cong 7.6 \cdot 10^{20}$ keV $\cdot$ m^{-3} constant
Temperature profile	flat

Table V: Background-plasma parameters for the W7-X case

Major radius R_0/m	5.5
Minor radius a/m	0.53
Mode numbers (m_1, n_1) and (m_2, n_2)	$(11, 10)$ and $(12, 10)$ toroidal coupl.
Magnetic field B_0/T on axis	2.31
Type of ions	hydrogen
Density $n_{\text{bulk},0}$/m^{-3} on axis	$2.0 \cdot 10^{19}$
Density profile	flat
q-profile	$q(r) = \sum_{i=0}^{6} c_i r^{2i}$
Coefficients	$c_0 = 1.175, c_1 = 0.521, c_2 = -13.150$ $c_3 = 101.17, c_4 = -435.05, c_5 = 947.01$ $c_6 = -831.19$

Table VI: Fast-particle parameters for the W7-X case

Type of ions	hydrogen
Density $N_{\text{fast},0}$/m^{-3} on axis	$4.0 \cdot 10^{17} \ldots 3.0 \cdot 10^{18}$
Density profile	$N_{\text{fast}}(r) = \sum_{i=0}^{9} c_i r^{2i}$
Coefficients	$c_0 = 0.99988, c_1 = -4.5984$ $c_2 = 42.474, c_3 = -473.91$ $c_4 = 606.59, c_5 = 66734$ $c_6 = -855490, c_7 = 4647400$ $c_8 = -11936000, c_9 = 11835000$
Temperature $T_{\text{fast},0}$/keV on axis	$10 \ldots 1000$
Temperature profile	flat

References

[1] M. N. Rosenbluth and P. H. Rutherford, Physical Review Letters **34**, 1428 (1975).

[2] G. Y. Fu and J. W. van Dam, Physics of Fluids B **1**, 1949 (1989).

[3] H. H. Duong, W. W. Heidbrink, E. J. Strait, T. W. Petrie, R. Lee, R. A. Moyer, and J. G. Watkins, Nuclear Fusion **33**, 749 (1993).

[4] R. B. White, E. Fredrickson, D. Darrow, M. Zarnstorff, R. Wilson, S. Zweben, K. Hill, Y. Chen, and G. Fu, Physics of Plasmas **2**, 2871 (1995).

[5] L. Chen, Physics of Plasmas **1**, 1519 (1994).

[6] P. Lauber and S. Günter, Nuclear Fusion **48**, 084002 (2008).

[7] A. H. Boozer, Review of Modern Physics **76**, 1071 (2004).

[8] H. L. Berk, J. W. van Dam, Z. Guo, and D. M. Lindberg, Physics of Fluids B **4**, 1806 (1992).

[9] Y. I. Kolesnichenko, V. V. Lutsenko, H. Wobig, Y. V. Yakovenko, and O. P. Fesenyuk, Physics of Plasmas **8**, 491 (2001).

[10] Y. I. Kolesnichenko, V. V. Lutsenko, H. Wobig, and Y. V. Yakovenko, Nuclear Fusion **42**, 949 (2002).

[11] A. Könies and R. Kleiber, Physics of Plasmas **19**, 122111 (2012).

[12] A. Könies, Physics of Plasmas **7**, 1139 (2000).

[13] G. Y. Fu, H. L. Berk, and A. Pletzer, Physics of Plasmas **12**, 082505 (2005).

[14] P. Rodrigues, A. Figueiredo, J. Ferreira, R. Coelho, F. Nabais, D. Borba, N. F. Loureiro, H. J. C. Oliver, and S. E. Sharapov, Nuclear Fusion **55**, 083003 (2015).

[15] T. H. Stix, *Waves in Plasmas* (American Institute of Physics, 1992).

[16] M. R. Scott, Journal of Computational Physics **12**, 334 (1973).

[17] D. M. Sloan, Journal of Computational Physics **24**, 320 (1977).

[18] J. Candy and M. N. Rosenbluth, Plasma Physics and Controlled Fusion **35**, 957 (1993).

[19] M. Fivaz, S. Brunner, G. de Ridder, O. Sauter, T. M. Tran, J. Vaclavik, L. Villard, and K. Appert, Computer Physics Communications **111**, 27 (1998).

[20] A. Mishchenko, R. Hatzky, and A. Könies, Physics of Plasmas **11**, 5480 (2004).

[21] A. Mishchenko, A. Könies, and R. Hatzky, Physics of Plasmas **16**, 082105 (2009).

[22] A. Könies, S. Briguglio, N. Gorelenkov, T. Fehér, M. Isaev, P. Lauber, A. Mishchenko, D. A. Spong, Y. Todo, W. A. Cooper, et al. (24th IAEA Int. Conf. on Fusion Energy (San Diego, CA, 2012), 2012), `http://www-naweb.iaea.org/napc/physics/FEC/FEC2012/papers/437_ITRP134.pdf`.

[23] A. Könies, A. Mishchenko, and R. Hatzky, in *Theory of Fusion Plasmas*, edited by X. Garbet, O. Sauter, and E. Sindoni (American Institute of Physics, New York, 2008), vol. 1069, pp. 133–143.

[24] T. B. Fehér, Ph.D. thesis, Ernst-Moritz-Arndt-Universität Greifswald (2013).

[25] N. N. Gorelenkov, C. Z. Cheng, and G. Y. Fu, Physics of Plasmas **6**, 2802 (1999).

[26] H. Qin, W. M. Tang, and G. Rewoldt, Physics of Plasmas **6**, 2544 (1999).

[27] G. Y. Fu, C. Z. Cheng, and K. L. Wong, Physics of Fluids B **5**, 4040 (1993).

[28] P. Lauber, S. Günter, A. Könies, and S. D. Pinches, Journal of Computational Physics **226**,

447 (2007).
[29] W. Baumjohann and R. A. Treumann, *Basic Space Plasma Physics* (Imperial College Press, 1997).
[30] Y. I. Kolesnichenko, V. V. Lutsenko, H. Wobig, and V. Yakovenko, Physics of Plasmas **9**, 517 (2002).
[31] S. Briguglio, X. Wang, F. Zonca, G. Vlad, G. Fogaccia, C. D. Troia, and V. Fusco, Physics of Plasmas **21**, 112301 (2014).